Supplement of Atmos. Chem. Phys., 19, 8425–8470, 2019
https://doi.org/10.5194/acp-19-8425-2019-supplement

Atmospheric Chemistry and Physics
Open Access
EGU

Supplement of

Land cover and its transformation in the backward trajectory footprint region of the Amazon Tall Tower Observatory

Christopher Pöhlker et al.

Correspondence to: Christopher Pöhlker (c.pohlker@mpic.de)

This file includes:

Supplementary information relating to methods and data analysis

Tables S1 to S2

Figs. S1 to S20

References

S1 Supplementary information relating to methods and data analysis

S1.1 List of GIS datasets used in this study

In this study, the following GIS data sets were used:

(i) Landscape topography: Surface elevation data was obtained from the Shuttle Radar Topography Mission (SRTM) at 3 arc-seconds of spatial resolution (Farr et al., 2007). The data is assessable via the following link: https://www2.jpl.nasa.gov/srtm/southAmerica.htm (last access 02 Dec 2017).

(ii) Mean air temperature and annual precipitation: Mean air temperature and annual precipitation grid layers were obtained from the WorldClim database, version 1.4, at 10 arc-minute resolutions, available under www.worldclim.org (last access 27 Nov 2017) (Hijmans et al., 2005). The datasets were obtained by interpolation of the major long-term periods in climate databases (mostly for the 1950–2000 period), such as the Global Historical Climatology Network (GHCN), the Food and Agriculture Organization (FAO) of the United Nations, the World Meteorological Organization (WMO), the International Center for Tropical Agriculture (CIAT), R-HYdronet, among others. Spatial interpolation was done using the thin-plate smoothing spline algorithm (Hutchinson, 2004) and the 3 arc-seconds digital elevation model obtained from the SRTM and the ANUSPLIN software (see Hijmans et al., 2005 for further details).

(iii) Biomes and ecoregions: The biome and ecoregion classification in this study is based on the work by Olson et al. (2001). It is freely provided by the World Wildlife Fund (WWF) under https://www.worldwildlife.org/publications/terrestrial-ecoregions-of-the-world (last access 25 Feb 2018). This dataset specifies 867 different ecoregions worldwide in 14 different biomes (e.g., forest, grassland, desert, etc.).

(iv) Köppen-Geiger climate classification: The maps used in this study represent an update by Kottek et al. (2006) and Rubel and Kottek (2010) of the original classification maps. The data was obtained from http://koeppen-geiger.vu-wien.ac.at/shifts.htm (last access 25 Feb 2018).

(v) Human footprint and the last of the wild: The global maps on the human footprint index and areas with the "last of the wild" are based on the study by Sanderson et al. (2002). The areas with the "last of the wild" are characterized by the lowest human influences index and represent the "10 % wildest areas in each biome in each realm around the world" (Sanderson et al., 2002).

(vi) Potential vegetation: The potential vegetation coverage, which represents the land cover and natural vegetation in the absence of human alteration, was obtained from the International Satellite Land-Surface Climatology Project, Initiative II (ISLSCP II) data collection (Ramankutty and Foley, 2010). The data set is available online under http://daac.ornl.gov/ (last access 25 Feb 2018).

(vii) Land cover: The land cover data in this study is based on the GlobCover 2009 data set, provided by the European space agency (ESA) and several partners (Arino et al., 2008). The data is freely

available under http://due.esrin.esa.int/page_globcover.php (last access 25 Feb 2018). It provides 22 land cover classes, which are compatible with the UN land cover classification (UNLC). The spatial resolution of the GlobCover pixels equal 300 m. The GlobCover 2009 data has been obtained in the period 1 Jan until 31 Dec 2009 (Congalton et al., 2014; Quaife and Cripps, 2016). An assessment of the geometric and thematic accuracy of the GlobCover 2009 data can be found in Defourny et al. (2009) documenting the generally high quality of the data. However, the authors also point out that the input data coverage for certain areas Amazonia is comparatively low, which increases the uncertainty and has to be considered carefully.

(viii) Normalized Difference Vegetation Index (NDVI): To obtain information on vegetation seasonality we used the NDVI data (Rouse et al., 1973), which is a widely implemented remote sensing vegetation index. It is directly related to the fraction of photosynthetically active radiation intercepted by vegetation and can be used as a proxy of net primary productivity (Paruelo et al., 2001). Mean monthly NDVI values and standard deviations of the different land cover classes within the ROI_{foot} were calculated from 16 composite MOD13Q1, obtained from Google Earth Engine for the period 2001-2016.

(ix) Forest cover and forest loss: The GIS data on forest cover and forest loss are based on work by Hansen et al. (2013). The data is freely provided by the University of Maryland (USA) under https://earthenginepartners.appspot.com/science-2013-global-forest (last access 25 Feb 2018). The forest cover data represent the status in the year 2000 and is provided as percent of forest cover per pixel. The spatial resolution equals 30 m per pixel. The forest loss data, which includes any tree cover loss in primary and secondary forests, is available within the time period 2001-2014 and refers to the status in the year 2000. In this study, we use both, forest loss data as total forest loss (integrated from 2001 to 2014) as well as annual forest loss (annually resolved for the years 2001 until 2014). Besides the widely used forest loss data provided by the University of Maryland, other forest loss data products, such as the Brazilian national satellite-based deforestation monitoring system (PRODES, www.obt.inpe.br/prodes, last access 25 Feb 2017) as well as the studies by Souza et al. (2013) and Tyukavina et al. (2017), are available. Note that these different forest loss datasets agree on the overall trends, however, deviate to some extent in certain aspects, which can be explained by different methodological approaches (for details, see Tyukavina et al., 2017 and references therein). A limitation of the forest loss data used in this work is the fact that non-stand-replacement disturbances (i.e., selective logging, fire-related increases in forest vulnerability, etc.) are not included (Tyukavina et al., 2017).

(x) Fire maps: Two satellite-derived datasets on fire occurrence in the Amazon Basin were used in this study: First, fire-related carbon emission flux data based on Moderate Resolution Imaging Spectroradiometer (MODIS) observations has been obtained from the Global Fire Assimilation System (GFAS), available under http://eccharts.ecmwf.int/datasets/data/cams-gfas/ (last access

25 Feb 2018). This data is shown as average carbon emission flux data spanning from 2003-2017 in Fig. 15. Moreover, anomalies in carbon emission flux for individual years relative to the multi-year average (2003-2017) have been calculated (see Fig. S19). For details, refer to Kaiser et al. (2012). Second, data on detected fires based on multiple space-borne instruments (including MODIS) have been obtained from the Instituto Nacional de Pesquisas Espaciais (INPE), available under https://prodwww-queimadas.dgi.inpe.br/bdqueimadas (last access 25 Feb 2018). The INPE data has been downloaded for all available satellites, covering the entire continent and spanning the time period from Jan 2000 to Dec 2016. Note, the INPE data does not specify the fire intensity. It was used in this study to calculate a fire count per pixel as shown in Fig. S17. Multi-year average INPE and GFAS fire maps show similar geospatial distributions of fire occurrence and, thus, underline a good agreement of both data products.

(xi) Protected areas and conservations: The GIS data on conserved areas in the context of this study is based on the World Database on Protected Areas (WDPA), which has been created jointly by the International Union for Conservation of Nature (UICN), the United Nations Environment Program (UNEP), and partners (https://www.protectedplanet.net/, last access 25 Feb 2018).

(xii) Land-based travel times to the nearest densely-populated area: This data is based on a study by Weiss et al., (2018) and constitutes the basis for the 'remoteness map' in Fig. 20b. The data has been obtained from Google Earth Engine under https://code.earthengine.google.com/ (last access 25 Feb 2018).

(xiii) Population density: The gridded population of the world data (version 4, GPWv4) has been compiled by the Center for International Earth Science Information Network (CIESIN), Columbia University, USA, and has been distributed by via the NASA SEDAC webpage (http://beta.sedac.ciesin.columbia.edu/data/set/gpw-v4-population-density-rev10, last access 25 Feb 2018). The data set used here, reflects the status in the year 2015. A detailed documentation can be found under http://dx.doi.org/10.7927/H4D50JX4 (last access 25 Feb 2018).

(xiv) Roads: The GIS information on highways and roads in the Amazon Basin were retrieved from the OpenStreetMap (OSM) data set, which is available via https://www.openstreetmap.org (last access 24 Feb 2018). The OSM data used here were released on 23 Feb 2018. The metadata specifies the type of roads. In the context of this study, we displayed primary, secondary, and tertiary roads as well as proposed new roads in the corresponding maps. We further used GIS data on the Amazonian road network from CRS maps, available under http://maps.csr.ufmg.br/ (last access 24 Feb 2018). The CRS data provided information on highway pavement status.

(xv) Power plants: The locations of thermoelectric power plots has been obtained from https://sigel.aneel.gov.br/Down/ (last access 25 Feb 2018).

(xvi) Reservoirs and dams: The global reservoir and dam dataset (GRanD) is based on a work by Lehner et al. (2011). The data has been obtained from the NASA SEDAC webpage

(http://sedac.ciesin.columbia.edu/data/set/grand-v1-reservoirs-rev01 and http://sedac.ciesin.columbia.edu/data/set/grand-v1-dams-rev01, last access 25 Feb 2018).

(xvii) Mining: The GIS data on mining has been obtained from Sistema de Informações Geográficas da Mineração (SIGMINE) under http://sigmine.dnpm.gov.br/webmap/ (last access 04 Mar 2018). Note that this data is only available for Brazil.

(xviii) Shipping: Ship tracks in this study are represented by the geospatial information on shipping-related CO_2 emissions from the fossil fuel data assimilation system (FFDAS). The data is freely accessible under http://hpcg.purdue.edu/FFDAS/Map.php (last access 25 Feb 2018). Further information on the FFDAS data can be found in Rayner et al., (2010) and Asefi-Najafabady et al. (2014).

(xix) Deforestation scenarios: The deforestation scenarios used here are based on a modelling study on future deforestation patterns in the Amazon basin, spanning from 2002 to 2050. The study was conducted in the context of the large-scale biosphere-atmosphere experiment in the Amazon (LBA). The data has been compiled by Soares-Filho et al. (2013) and has been obtained from https://daac.ornl.gov/cgi-bin/dsviewer.pl?ds_id=1153 (last access 25 Feb 2018). It is available as "governance" and "business as usual (BAU)" scenarios. Further information can be found in Soares-Filho et al. (2006).

Table S1. The land cover contributions according the GlobCover 2009 data, resolved by BT clusters and weighted by air mass residence time. The data summarized here is plotted in Fig. 11.

GlobCover categories	NE				ENE					E					ESE				SW1	Av
	NE1	NE2	NE3	Av	ENE	ENE	ENE	ENE	Av	E1	E2	E3	E4	Av	ESE1	ESE2	ESE3	Av		all
11	0	0	0	**0**	0	0	0	0	**0**	0	0	0	0	**0**	0	0	0	**0**	0	**0**
14	0.001	0.001	0.002	**0.001**	0.001	0.009	0.007	0.005	**0.006**	0.017	0.143	0.226	0.524	**0.228**	1.177	3.419	3.370	**2.655**	0.035	**0.596**
20	0.250	0.164	0.150	**0.188**	0.730	0.895	0.727	0.502	**0.714**	1.910	2.983	2.117	2.055	**2.266**	3.143	6.593	9.084	**6.273**	0.850	**2.144**
30	0.185	0.121	0.095	**0.134**	0.340	0.294	0.229	0.153	**0.254**	0.900	1.689	1.684	1.988	**1.565**	1.340	4.484	8.006	**4.610**	0.306	**1.454**
40	74.79	47.95	37.95	**53.56**	86.11	54.88	43.16	34.20	**54.59**	65.75	49.53	38.42	32.84	**46.64**	83.16	68.48	55.79	**69.14**	84.84	**57.19**
50	0.001	0.001	0.002	**0.001**	0.001	0.005	0.003	0.003	**0.003**	0.003	0.092	0.045	0.054	**0.049**	0.562	0.942	1.183	**0.896**	0.011	**0.194**
60	0	0	0	**0**	0	0	0	0	**0**	0.001	0.030	0.091	0.104	**0.057**	0.022	0.428	0.766	**0.405**	0	**0.096**
70	0	0	0	**0**	0	0	0	0	**0**	0	0	0	0	**0**	0	0	0	**0**	0	**0**
90	0	0	0	**0**	0	0	0	0	**0**	0	0	0	0	**0**	0	0	0	**0**	0	**0**
100	0	0	0	**0**	0	0	0	0	**0**	0	0	0	0	**0**	0	0	0	**0**	0	**0**
110	0.051	0.039	0.042	**0.044**	0.206	0.219	0.152	0.102	**0.170**	0.551	0.525	0.500	0.516	**0.523**	0.113	0.274	0.726	**0.371**	0.094	**0.274**
120	0	0	0	**0**	0.002	0.008	0.007	0.004	**0.005**	0.006	0.008	0.015	0.018	**0.012**	0.002	0.007	0.035	**0.015**	0.017	**0.009**
130	1.784	1.193	0.961	**1.313**	2.013	1.486	1.098	0.776	**1.343**	2.920	3.916	3.242	3.048	**3.282**	1.621	5.139	11.38	**6.047**	0.942	**2.768**
140	0.202	0.145	0.119	**0.155**	0.498	0.287	0.190	0.130	**0.276**	0.655	0.481	0.303	0.217	**0.414**	0.337	0.423	0.343	**0.368**	0.558	**0.326**
150	0	0	0	**0**	0	0	0	0	**0**	0	0.015	0.020	0.021	**0.014**	0.001	0.005	0.016	**0.007**	0	**0.005**
160	1.259	0.843	0.662	**0.921**	2.267	2.413	1.944	1.335	**1.990**	7.317	7.259	5.107	4.121	**5.951**	2.049	2.126	2.201	**2.125**	4.653	**3.037**
170	0.007	0.007	0.005	**0.006**	0.001	0.005	0.004	0.003	**0.003**	0.029	0.426	0.287	0.224	**0.242**	0	0.044	0.118	**0.054**	0	**0.077**
180	0.922	0.626	0.488	**0.679**	2.781	1.202	0.812	0.540	**1.334**	3.520	2.562	1.450	1.029	**2.140**	2.476	2.629	2.108	**2.404**	3.005	**1.743**
190	0.001	0.001	0	**0.001**	0.006	0.006	0.003	0.003	**0.005**	0.015	0.018	0.018	0.021	**0.018**	0.001	0.006	0.012	**0.006**	0.055	**0.011**
200	0	0	0	**0**	0.017	0.003	0.001	0	**0.005**	0.019	0.062	0.095	0.092	**0.067**	0.012	0.023	0.048	**0.028**	0.009	**0.025**
210	20.55	48.92	59.52	**43.00**	5.034	38.29	51.67	62.25	**39.31**	16.39	30.26	46.38	53.13	**36.54**	3.981	4.978	4.817	**4.592**	4.621	**30.05**
220	0	0	0	**0**	0	0	0	0	**0**	0	0.002	0.001	0.001	**0.001**	0	0.001	0.001	**0.001**	0	**0**
230	0	0	0	**0**	0	0	0	0	**0**	0	0	0	0	**0**	0	0	0	**0**	0	**0**

Table S2. Weighted quantification of forest cover and forest loss within the footprints of the 15 back trajectory clusters as specified in Fig. 13. The data summarized in this table is visualized in Fig. S15.

		Clusters														
		NE1	**NE2**	**NE3**	**ENE1**	**ENE2**	**ENE3**	**ENE4**	**E1**	**E2**	**E3**	**E4**	**ESE1**	**ESE2**	**ESE3**	**SW1**
2000	Tree cover [%]	77.16	49.447	39.142	88.77	56.673	44.567	35.228	71.768	56.929	43.676	37.36	86.07	74.06	63.592	90.187
	Forest loss [%]	--	--	--	--	--	--	--	--	--	--	--	--	--	--	--
2001	Tree cover [%]	77.151	49.439	39.136	88.641	56.602	44.521	35.204	71.495	56.662	43.527	37.24	85.58	73.521	63.172	90.046
	Forest loss [%]	0.015	0.017	0.015	0.154	0.124	0.104	0.069	0.381	0.468	0.341	0.321	0.572	0.727	0.66	0.156
2002	Tree cover [%]	77.139	49.431	39.13	88.483	56.526	44.472	35.178	71.217	56.376	43.365	37.108	85.085	72.84	62.596	89.828
	Forest loss [%]	0.015	0.016	0.015	0.178	0.134	0.111	0.073	0.386	0.5	0.369	0.351	0.572	0.912	0.9	0.241
2003	Tree cover [%]	77.131	49.426	39.127	88.38	56.472	44.437	35.161	71.017	56.171	43.245	37.012	84.707	72.368	62.213	89.703
	Forest loss [%]	0.01	0.01	0.008	0.116	0.096	0.078	0.049	0.277	0.357	0.273	0.255	0.434	0.627	0.593	0.139
2004	Tree cover [%]	77.116	49.416	39.12	88.209	56.377	44.375	35.13	70.664	55.861	43.064	36.866	84.012	71.51	61.501	89.521
	Forest loss [%]	0.02	0.021	0.018	0.192	0.166	0.14	0.089	0.487	0.537	0.41	0.388	0.795	1.132	1.095	0.2
2005	Tree cover [%]	77.106	49.409	39.115	88.097	56.315	44.334	35.108	70.414	55.611	42.932	36.753	83.381	70.533	60.767	89.306
	Forest loss [%]	0.013	0.014	0.013	0.125	0.109	0.092	0.064	0.342	0.43	0.297	0.297	0.716	1.274	1.117	0.237
2006	Tree cover [%]	77.094	49.401	39.11	87.951	56.238	44.283	35.082	70.154	55.331	42.774	36.622	82.869	69.736	60.099	89.085
	Forest loss [%]	0.015	0.016	0.014	0.163	0.135	0.113	0.072	0.356	0.481	0.356	0.345	0.576	1.025	1.003	0.242
2007	Tree cover [%]	77.083	49.393	39.105	87.823	56.178	44.245	35.063	69.896	55.048	42.626	36.499	82.407	69.085	59.531	88.965
	Forest loss [%]	0.015	0.016	0.014	0.143	0.105	0.085	0.054	0.352	0.483	0.332	0.323	0.516	0.828	0.844	0.131
2008	Tree cover [%]	77.067	49.382	39.098	87.695	56.109	44.2	35.039	69.633	54.79	42.479	36.376	81.818	68.288	58.862	88.842
	Forest loss [%]	0.021	0.022	0.017	0.143	0.12	0.1	0.067	0.357	0.438	0.33	0.321	0.655	1.003	0.984	0.135
2009	Tree cover [%]	77.046	49.368	39.089	87.403	55.963	44.104	34.989	69.165	54.378	42.219	36.176	81.272	67.607	58.305	88.61
	Forest loss [%]	0.027	0.028	0.024	0.324	0.255	0.213	0.142	0.633	0.696	0.578	0.52	0.603	0.848	0.81	0.253
2010	Tree cover [%]	77.031	49.358	39.082	87.314	55.916	44.071	34.969	68.962	54.083	42.057	36.031	80.871	66.916	57.67	88.344
	Forest loss [%]	0.02	0.021	0.018	0.099	0.083	0.074	0.056	0.273	0.495	0.359	0.376	0.44	0.852	0.916	0.29
2011	Tree cover [%]	77.02	49.351	39.077	87.236	55.865	44.035	34.949	68.789	53.908	41.956	35.943	80.479	66.385	57.237	88.232
	Forest loss [%]	0.014	0.014	0.012	0.087	0.09	0.079	0.057	0.231	0.293	0.222	0.228	0.428	0.648	0.617	0.122
2012	Tree cover [%]	76.982	49.326	39.06	87.058	55.77	43.969	34.911	68.488	53.649	41.796	35.808	79.88	65.559	56.494	87.997
	Forest loss [%]	0.049	0.05	0.044	0.197	0.165	0.146	0.107	0.401	0.431	0.351	0.347	0.651	0.999	1.052	0.255
2013	Tree cover [%]	76.962	49.313	39.051	86.916	55.698	43.92	34.884	68.207	53.302	41.604	35.646	79.524	64.882	55.808	87.834
	Forest loss [%]	0.026	0.026	0.024	0.157	0.125	0.108	0.077	0.373	0.575	0.42	0.414	0.384	0.809	0.959	0.177
2014	Tree cover [%]	76.942	49.301	39.043	86.758	55.613	43.863	34.854	67.902	52.976	41.411	35.49	79.052	64.125	55.087	87.668
	Forest loss [%]	0.026	0.024	0.02	0.175	0.147	0.125	0.086	0.404	0.537	0.421	0.398	0.506	0.896	0.995	0.179

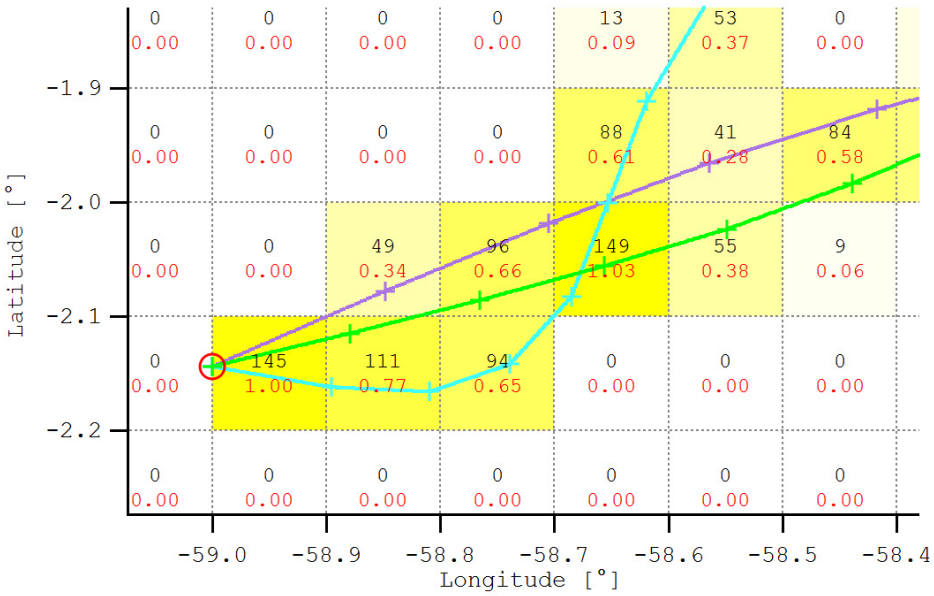

Figure S1. Sketch illustrating the weighting of the trajectory points, in this example for 3 trajectories (purple, green, cyan) starting at ATTO (red circle). The original trajectory points (crosses, time step 1 hour) are interpolated in order to get points on a 1-minute basis. Due to the interpolation of the hourly HYSPLIT output, the procedure weighted the individual trajectory points by residence time. The interpolated points are counted within a 0.1° by 0.1° grid (black numbers), e.g., 145 points within the grid besides ATTO. The absolute numbers are not very meaningful. For example, the numbers would be doubled in case of interpolating the trajectories to 0.5-minute steps instead on 1-minute steps, and they would be quadrupled in case of choosing a 2° by 2° grid for counting. To avoid this scaling issue, the absolute counts were divided by the counts in the grid pixel beside the ATTO site location (red numbers). These quotients we refer to as 'relative trajectory densities' and the resulting maps have been called ‘air mass residence time maps’. Slightly modified, this procedure can also be used to obtain averaged trajectory heights as well as average rainfall, mixing depth, etc.

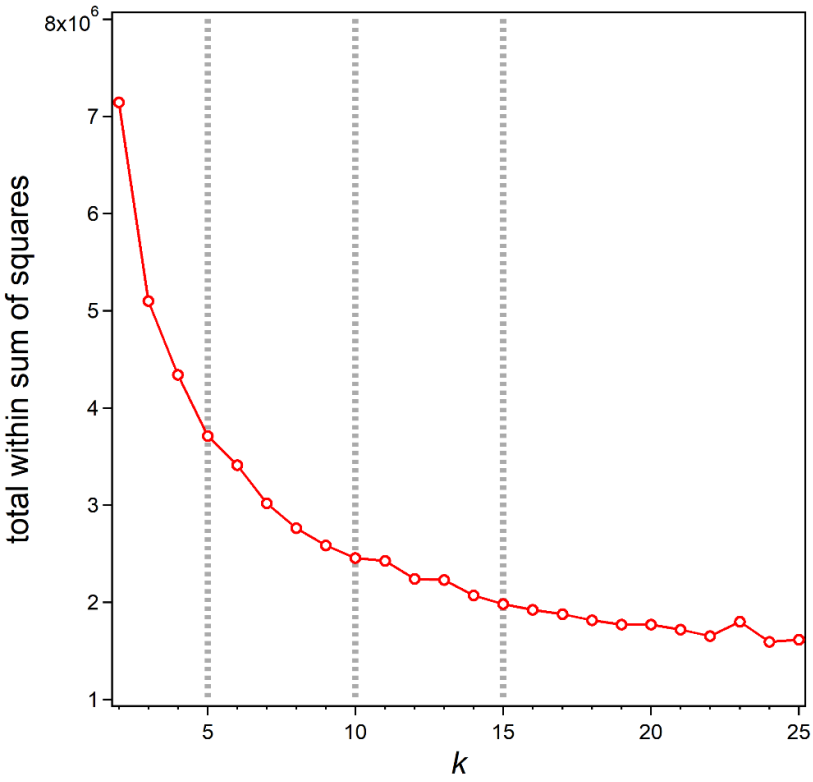

Figure S2. Total within-cluster sum of squares of *k*-means cluster analysis (CA) as a function of the pre-defined number of clusters, *k*. The 'elbow', which is not particularly pronounced here, is located in the range between $k = 5$ and $k = 10$. A comparison of *k*-means CA results for $k = 5$, 10, and 15 is shown in Fig. S3. For the systematic *k*-means CA in this study, $k = 15$, which is located after the elbow is reached, has been chosen for reasons outlined in Sect. 2.4.

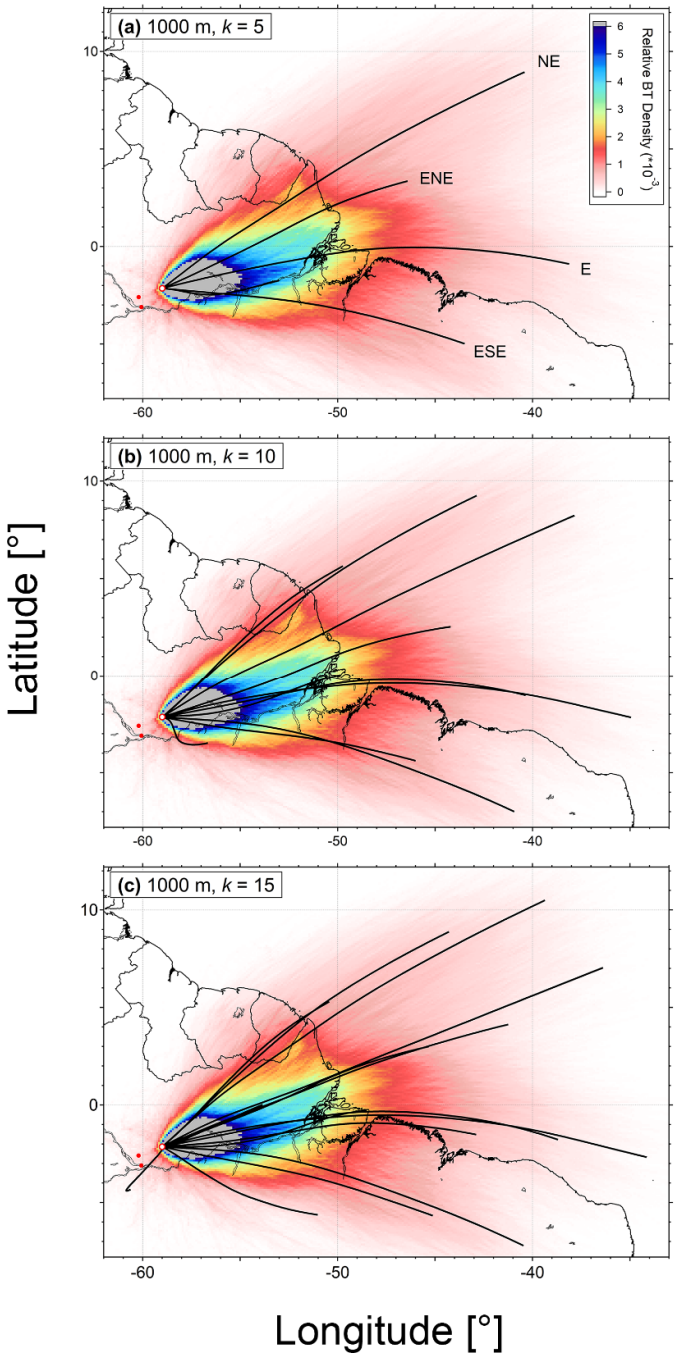

Figure S3. Air mass residence time maps, based on the entire ensembles of 3-day BTs (starting height 1000 m AGL, 01 Jan 2008 - 30 Jun 2016) with results from three *k*-means CA runs for $k = 5$, $k = 10$, and $k = 15$ (compare Fig. S2).

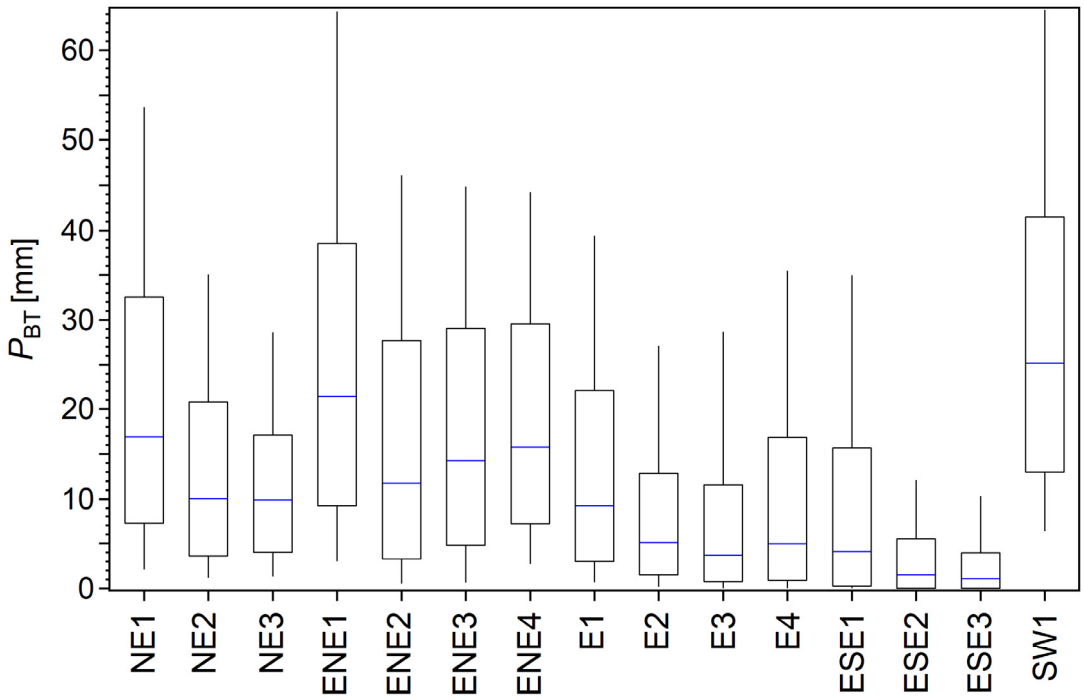

Figure S4. Statistical distribution (box and whisker plots) of cumulative precipitation, P_{BT}, for entire set of 74 496 3-day BTs, sorted by clusters. Results are based on k = 15 case (compare Fig. S2 and S3). Horizontal blue line represents median; lower and upper borders of box represents 25 and 75 percentiles. Whiskers represent 10 and 90 percentiles. Distributions show clearly enhanced P_{BT} for slow BT wind speed regimes (i.e., NE1, ENE1, E1, ESE1) in comparison to fast BT wind speed regimes (e.g., NE3, ENE3, E4, ESE3).

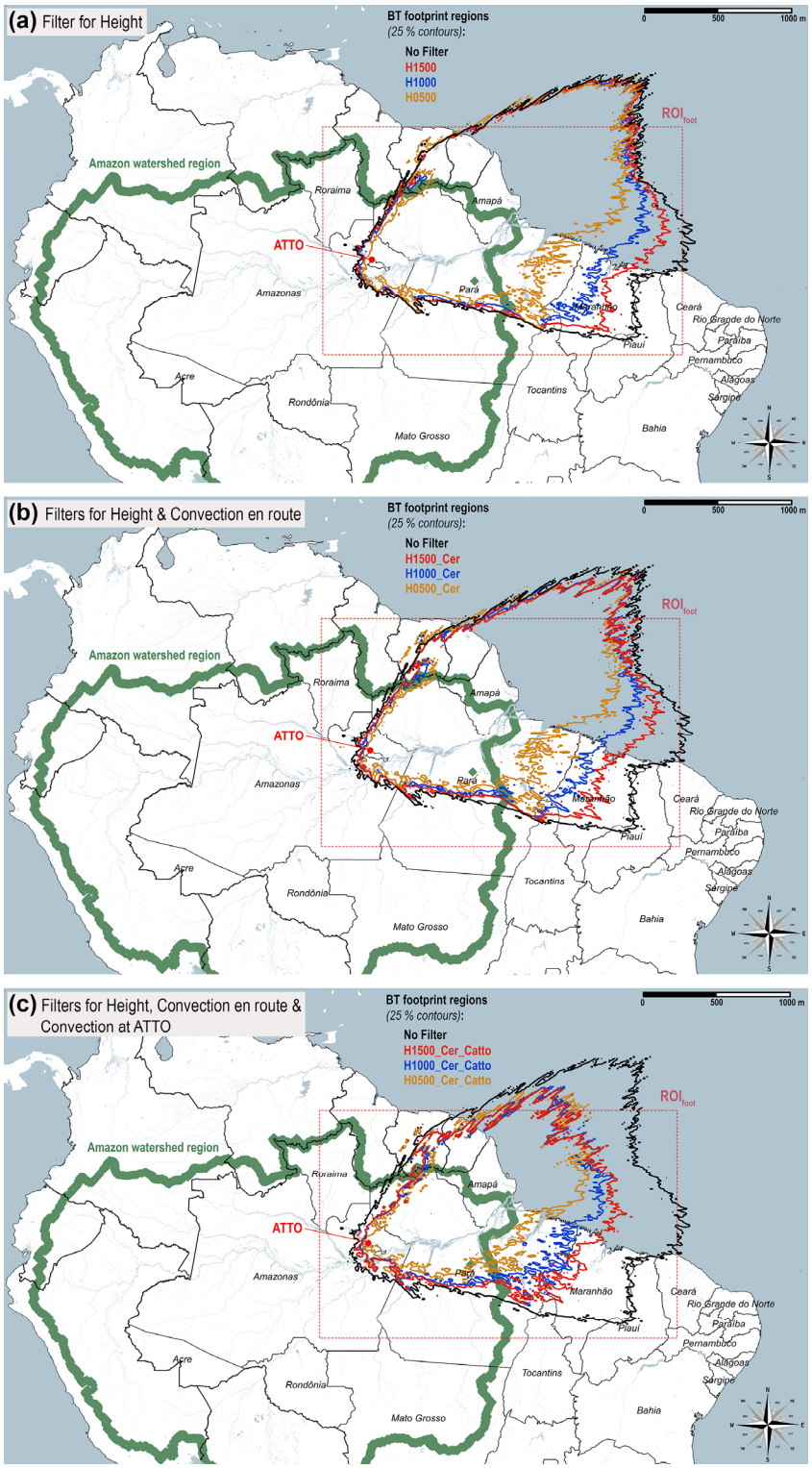

Figure S5. Versions of ATTO BT footprint region based on differently filtered BT ensembles as specified in Table 1 and discussed in Sect. 2.5 and 3.3.

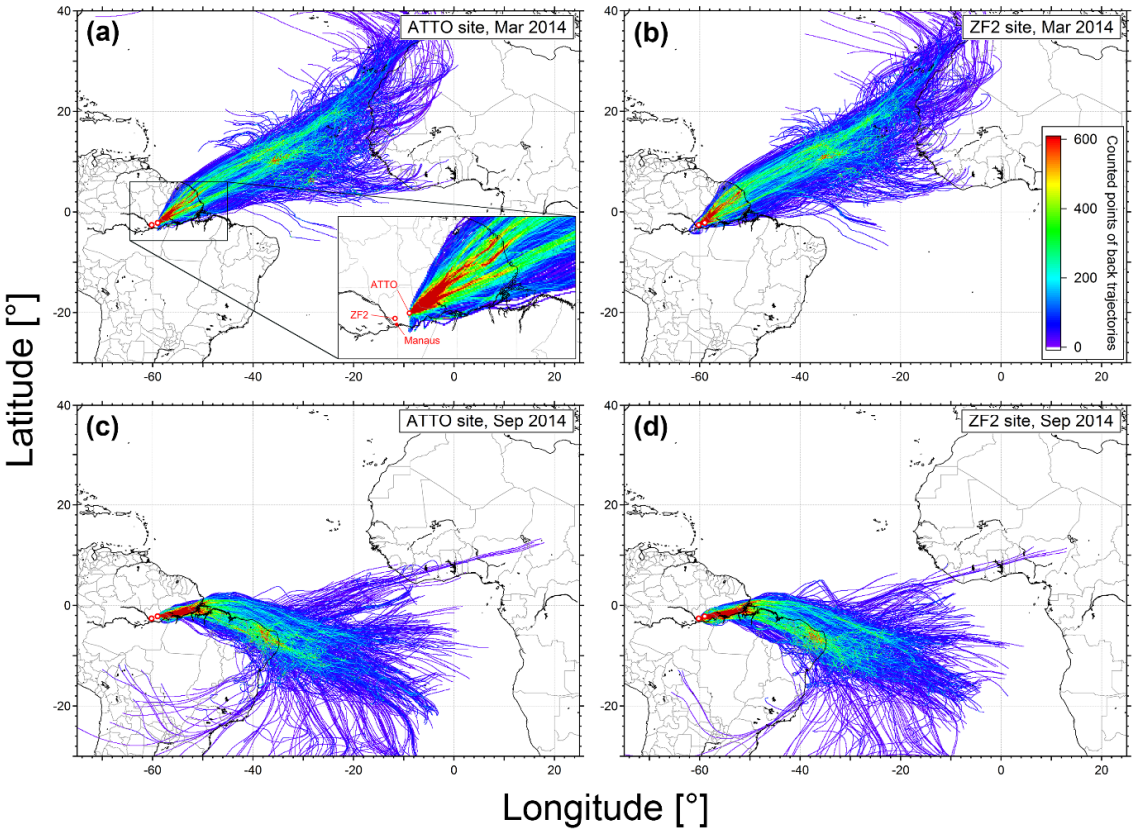

Figure S6. Comparison of 9-day HYSPLIT back trajectory (BT) ensembles for a selected wet season month (Mar 2014) and a selected dry season month (Sep 2014), underlining that large scale circulation patterns towards the Amazonian ATTO and ZF2 sites typically are very similar. Settings for BT calculations at both sites were identical (GDAS1, start height 1000 m AGL, trajectories started every 1 h). In this context, compare also Saturno et al. (2017).

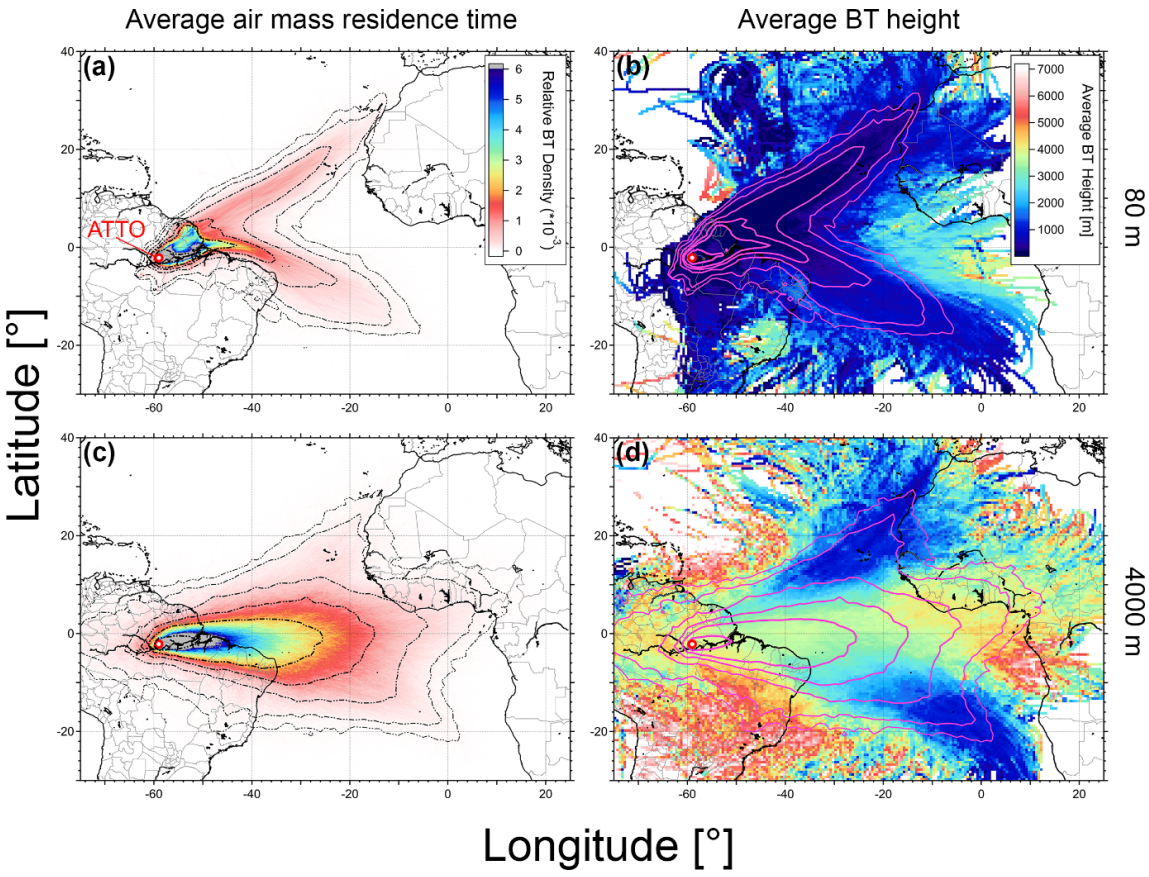

Figure S7. HYSPLIT back trajectory (BT) ensembles showing the large scale trade wind circulation in the Atlantic region and the seasonal oscillation between Northern and Southern hemispheric influence at ATTO by mean of air mass residence time maps (**a** and **c**) and average BT height maps (**b** and **d**). The BT ensembles comprise all 74 496 individual 9-day BTs, spanning a multi-year time period from 01 Jan 2008 until 30 June 2016. The BT analysis shown here was conducted for the start heights 80 m and 4000 m AGL. The contour lines in **b** and **d** were adopted from **a** and **c** to visualize the patterns in relative BT density on top of the average BT height map. Corresponding data for the BT start heights 200 m, 1000 m, and 2000 m can be found in Fig. 2.

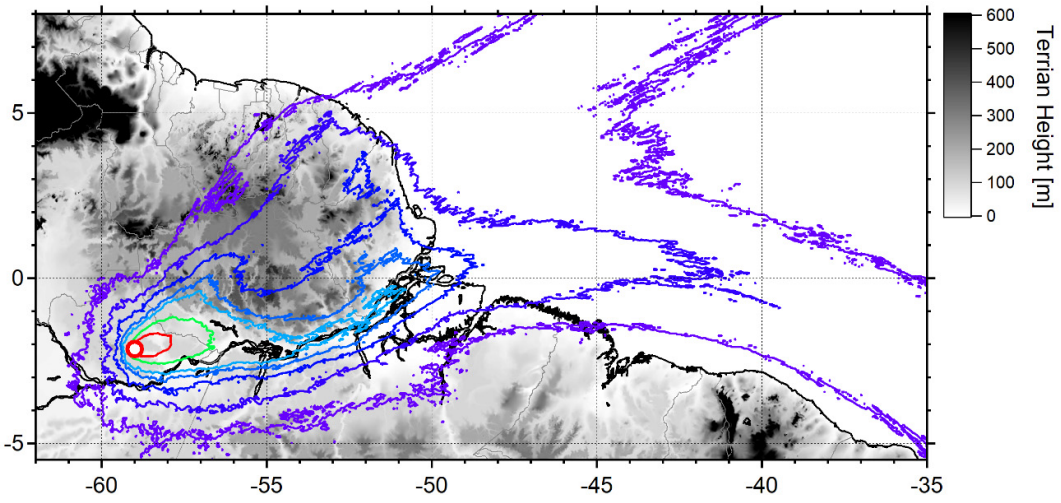

Figure S8. HYSPLIT back trajectory (BT) ensemble at start height of 200 m suggesting topography influence along the Amazon River valley.

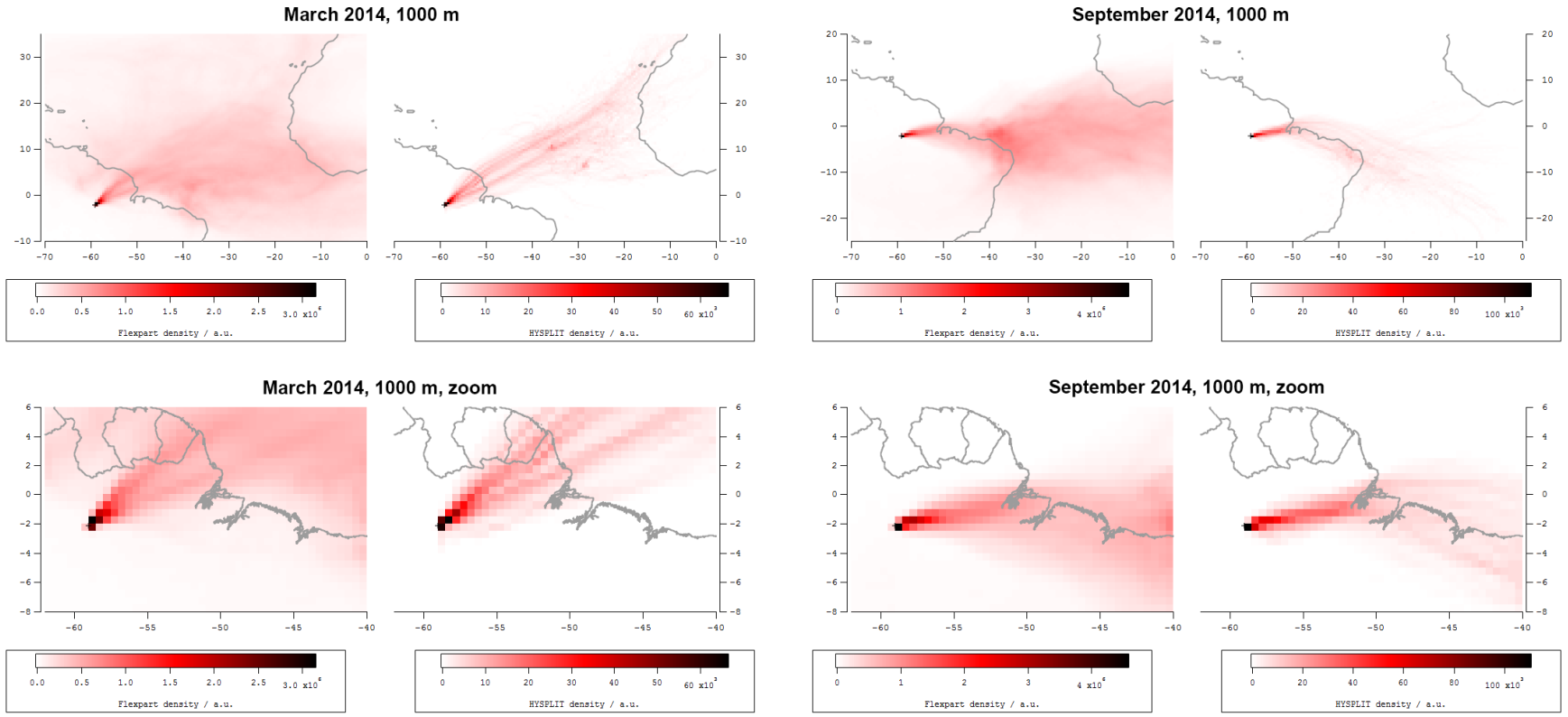

Figure S9. Alternative representation of FLEXPART and HYSPLIT back trajectory ensembles for wet season (Mar 2014, left) and dry season (Sep 2014, right) case studies as shown in Fig. 3. The color code represents relative BT density maps for both model. Top row shows results on a large-scale map (including NE South American and Western Africa). Bottom row shows same results as a zoomed map covering the NE Amazon Basin.

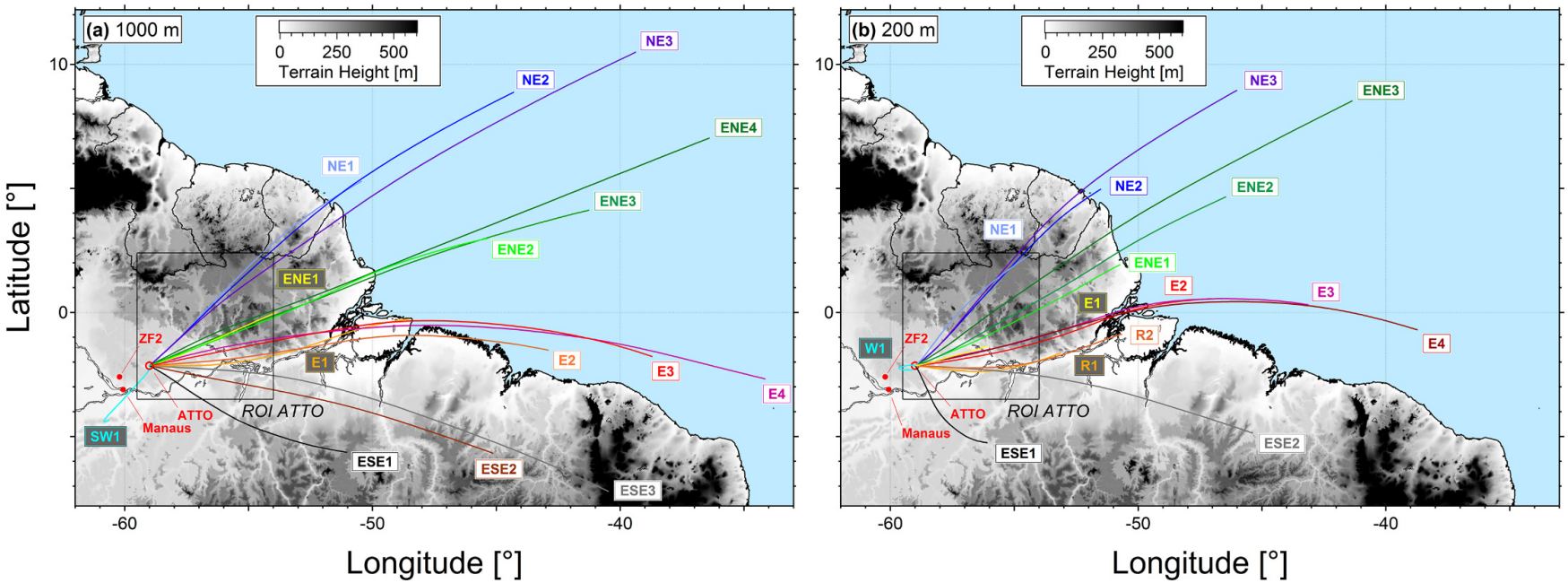

Figure S10. Map of northeast Amazon Basin with 15 clusters from systematic *k*-means back trajectory (BT) cluster analysis based on entire HYSPLIT data set (3-day BTs, 1 Jan 2008 - 30 Jun 2016). Here, the result from two different trajectory start heights are compared: 1000 m in (**a**) and 200 m AGL in (**b**). Throughout this study, the BT data set at 1000 m AGL is subject of a detailed analysis. The 1000 m case in (**a**) is identical to Fig. 4 and has been added here to allow a direct comparison. For the 200 m case, the cluster analysis has partitioned the individual BTs into four subcategories: (i) three NE clusters (i.e., NE1, NE2, NE3), (ii) three ENE clusters (i.e., ENE1, ENE2, ENE3), (iii) six easterly clusters (i.e., E1, E2, E3, E4) including two 'river trajectories' R1 and R2, and (iv) three inland trajectories (i.e., ESE1, ES2, W1). A topographic map is represented by a grey scale, which is capped at 600 m.

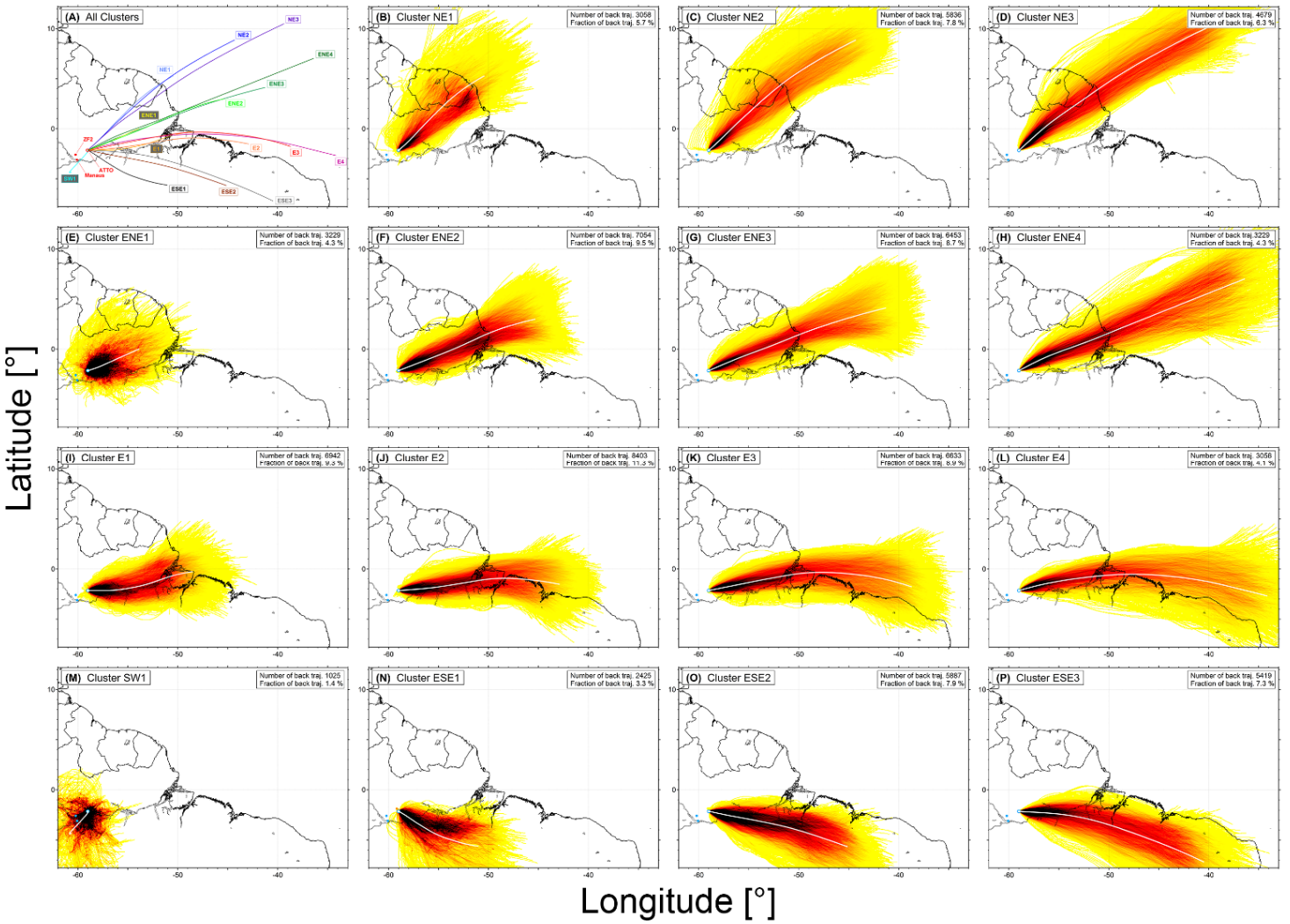

Figure S11. HYSPLIT back trajectory (BT) ensembles of the 15 clusters from the *k*-means cluster analysis (see Fig. 4). Individual maps show the average BT tracks (white lines) and the ensembles of all individual trajectories belonging to the respective clusters. The color code represents the average air mass residence time maps. The numbers *f* and *N* in the upper right corner of the individual panels specify for every cluster its relative fraction within the entire BT ensemble (74 496 individual BTs) as well as the absolute number of BTs included.

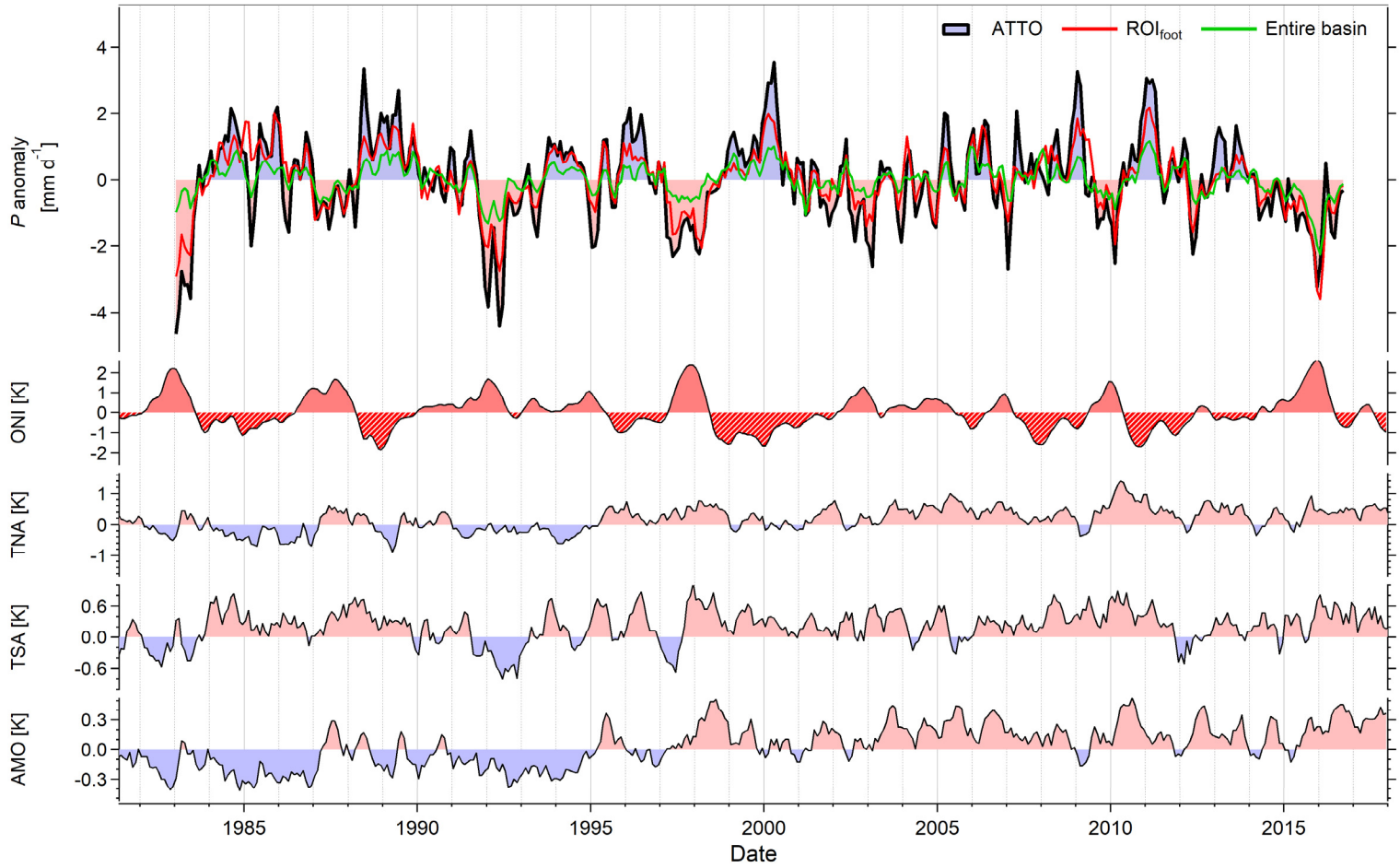

Figure S12. Anomalies in precipitation rate *P* for the ATTO region (see Fig. 4), the ROI$_{foot}$ (continental part only, see Fig. 4 and 7), and the entire basin (see Amazon watershed region in Fig. 7). Pacific and Atlantic sea surface temperature indices are shown for comparison: Oceanic Niño index (ONI), representing Pacific SST variability and indicating El Niño vs. La Niña periods (i.e., El Niño influence is very strong for ONI > 2.0, strong for 2.0 > ONI > 1.5, medium for 1.5 > ONI > 1.0, and weak for ONI > 1.0. La Niña influence is strong for -2.0 < ONI < -1.5, medium for -1.5 < ONI < -1.0, and weak for ONI > -1.0.). Tropical Northern Atlantic (TNA) and tropical Southern Atlantic (TSA) indices, representing Atlantic SST variability. Atlantic Multidecadal Oscillation (AMO) index.

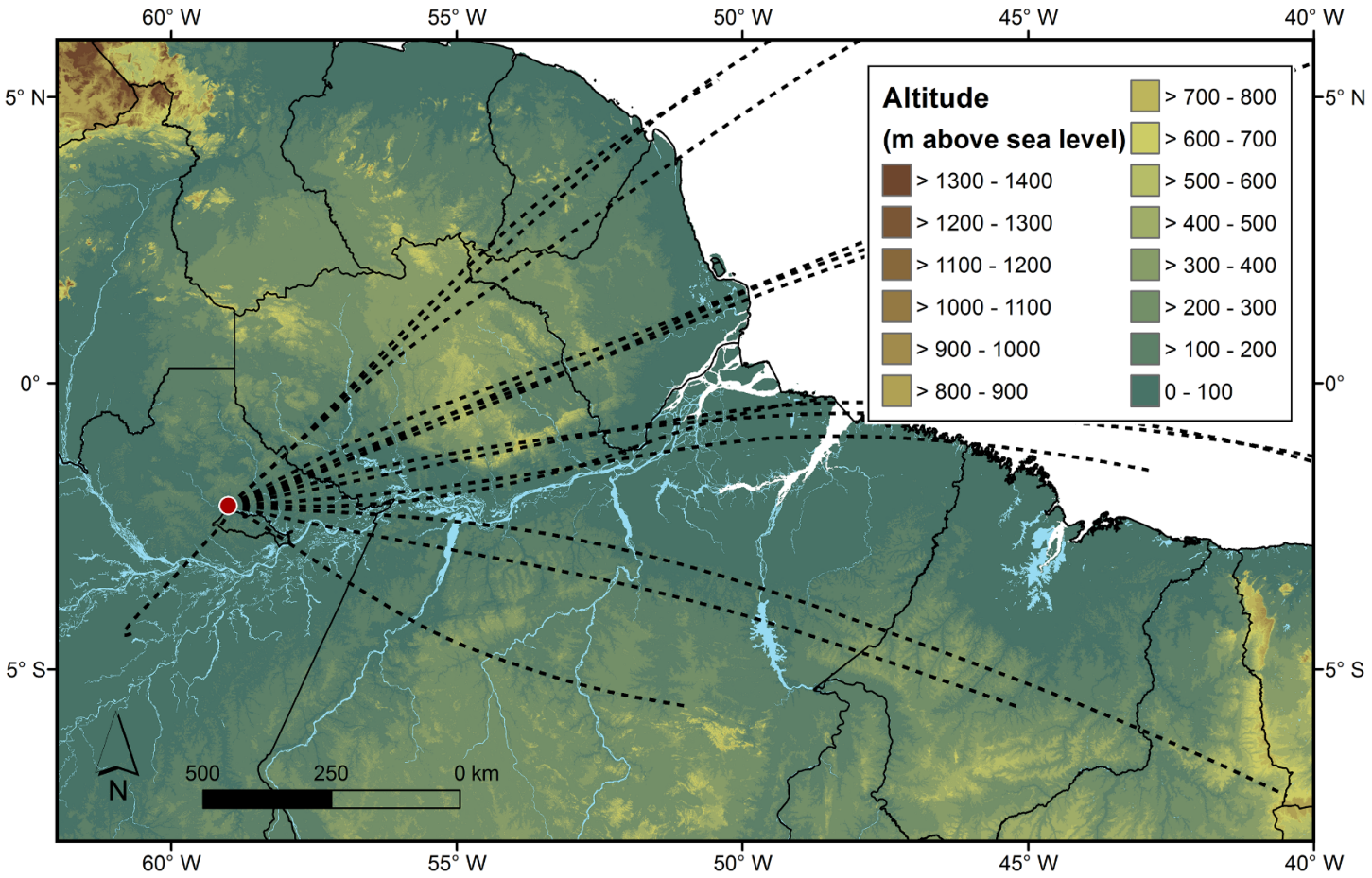

Figure S13. Map of the ATTO-relevant eastern Amazon Basin (ROI_{foot}) combining the backward trajectory (BT) data with altitude data obtained from SRTM digital elevation model. The trajectory data is represented as center lines of the 15 BT clusters (black dashed lines, see Fig. 4).

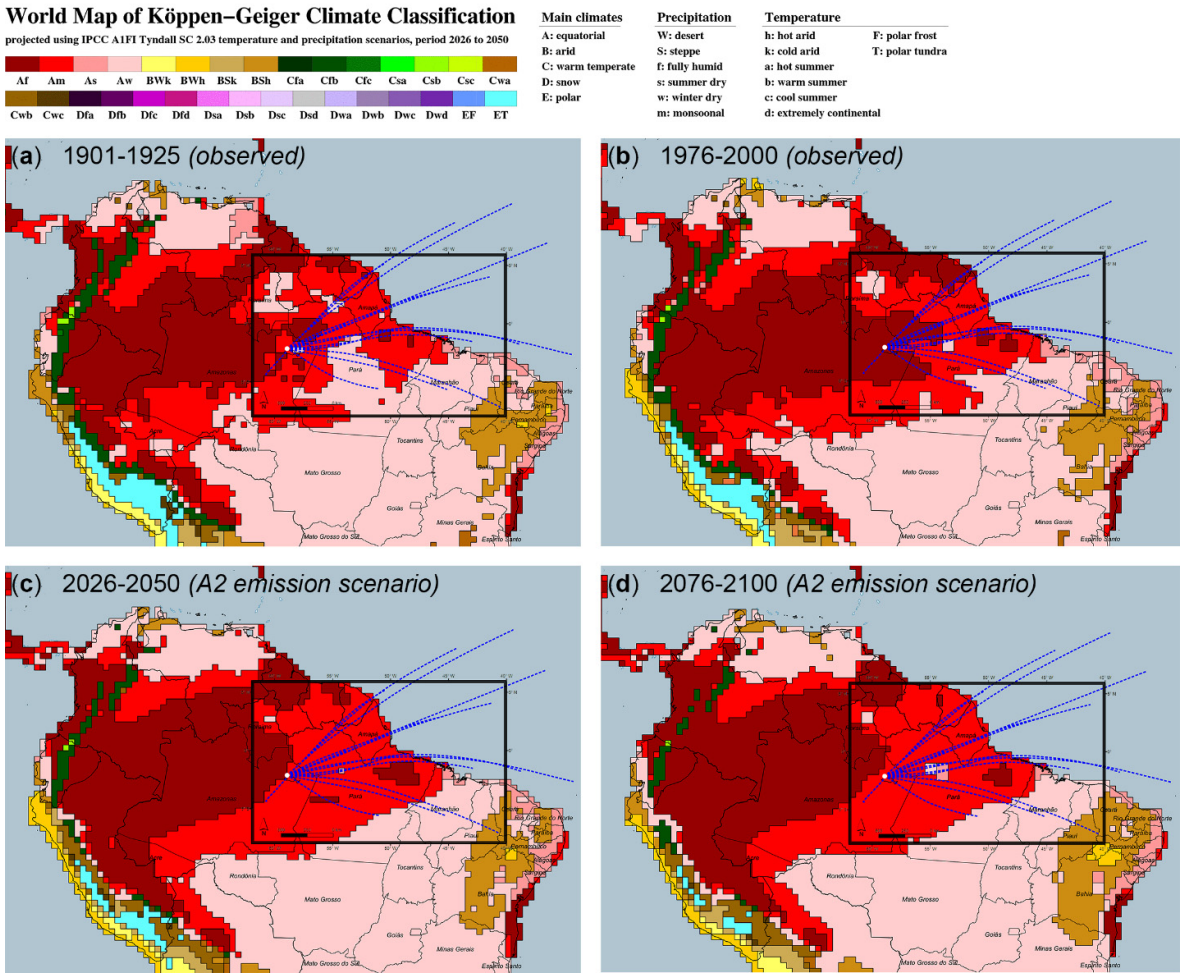

Figure S14. Map of the ATTO-relevant eastern Amazon Basin (ROI_{foot}) combining the backward trajectory (BT) data with the Köppen-Geiger climate classification for two observed periods (**a** and **b**), and projected based on the IPCC A2 emission scenario (**c** and **d**). The BT data is represented as center lines of the 15 BT clusters (blue dashed lines, see Fig. 4).

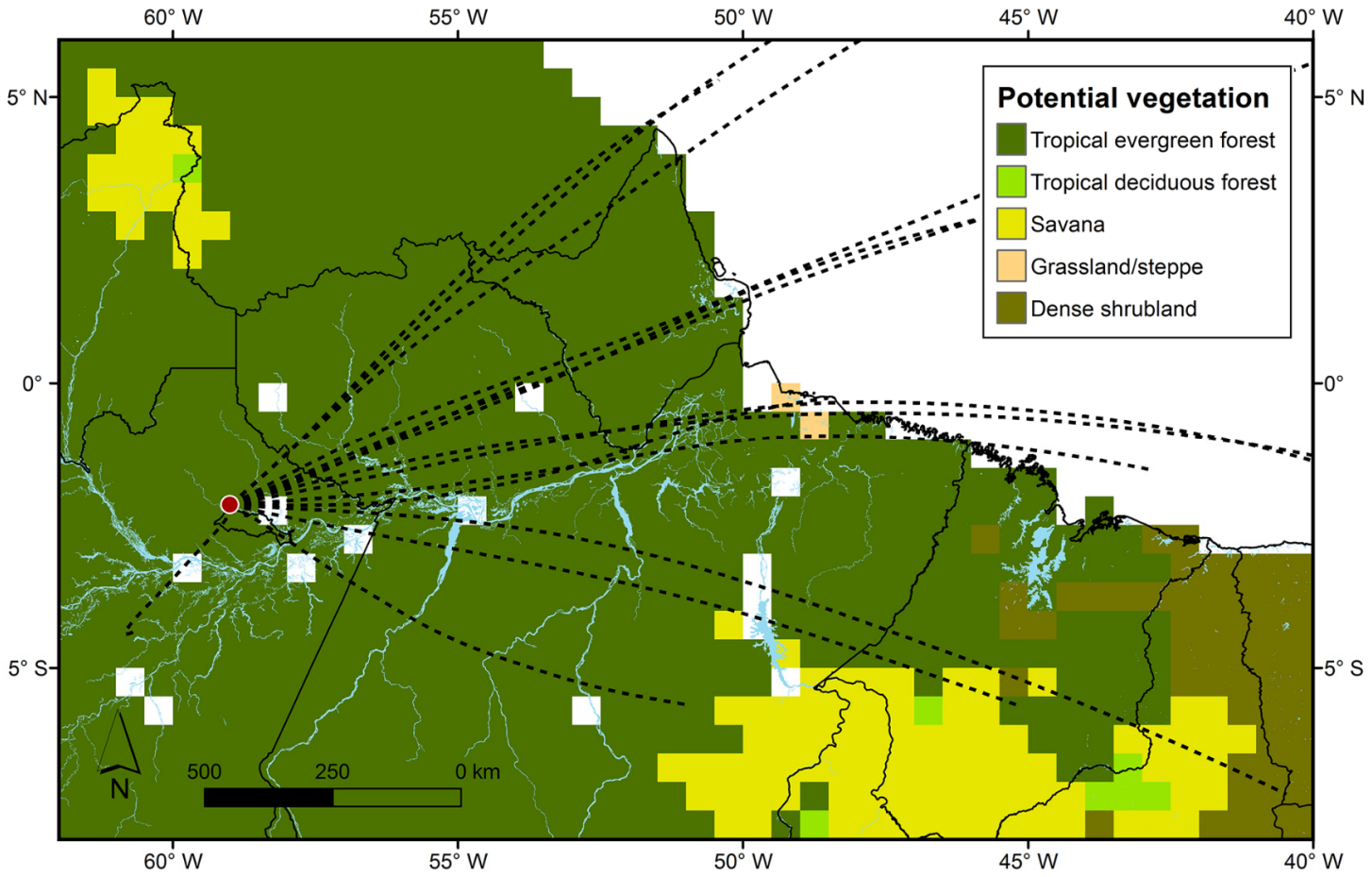

Figure S15. Map of the ATTO-relevant eastern Amazon Basin (ROI_{foot}) combining the backward trajectory (BT) data with GIS data representing potential nature vegetation coverage in the absence of human alteration, according to **(**Ramankutty and Foley., 2010**)**. The BT data is represented as center lines of the 15 BT clusters (black dashed lines, see Fig. 4).

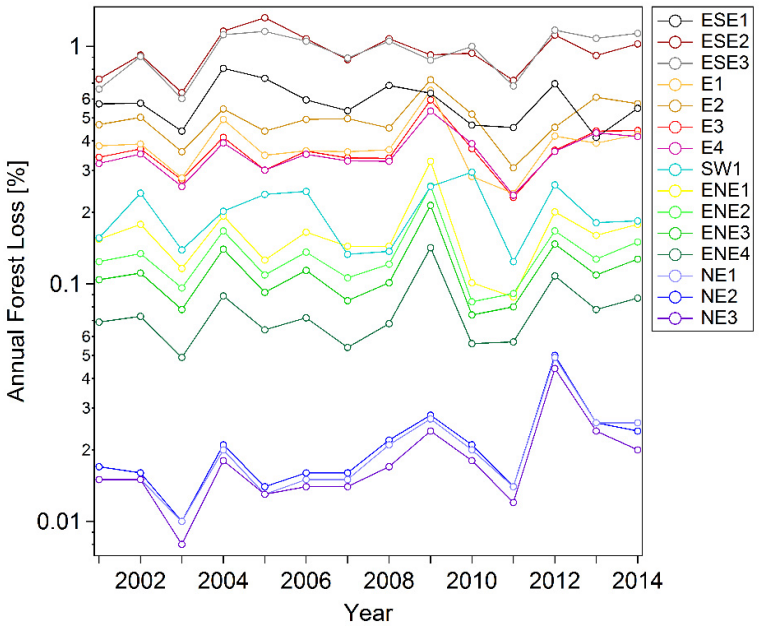

Figure S16. Quantitative characterization of forest loss trends (compare Fig. 13 and 14) in cluster BT footprints for all 15 clusters (see Fig. 4). The annual forest loss has been calculated relative to the forest cover in the year 2000. The forest loss data in the cluster BT footprints has been weighted by the air mass residence time.

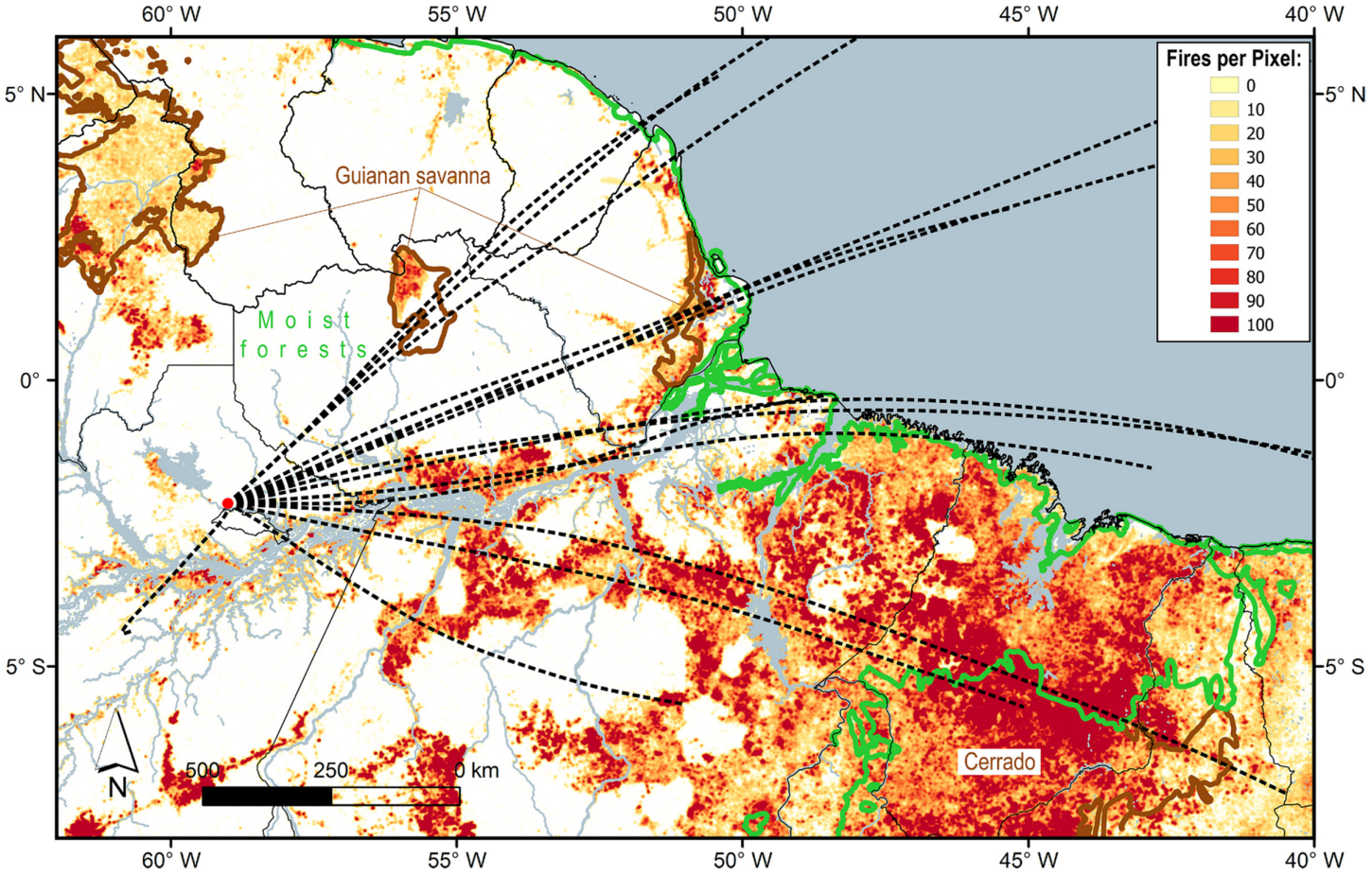

Figure S17. Map of the ATTO-relevant eastern Amazon Basin (ROI_{foot}) combining the backward trajectory (BT) data with two GIS data layer: (i) map of satellite detected fires within time period from 1998 to 2016 based on INPE data base and (ii) biome classification (see Fig. 9a). The BT data is represented as center lines of the 15 BT clusters (black dashed lines, see Fig. 4).

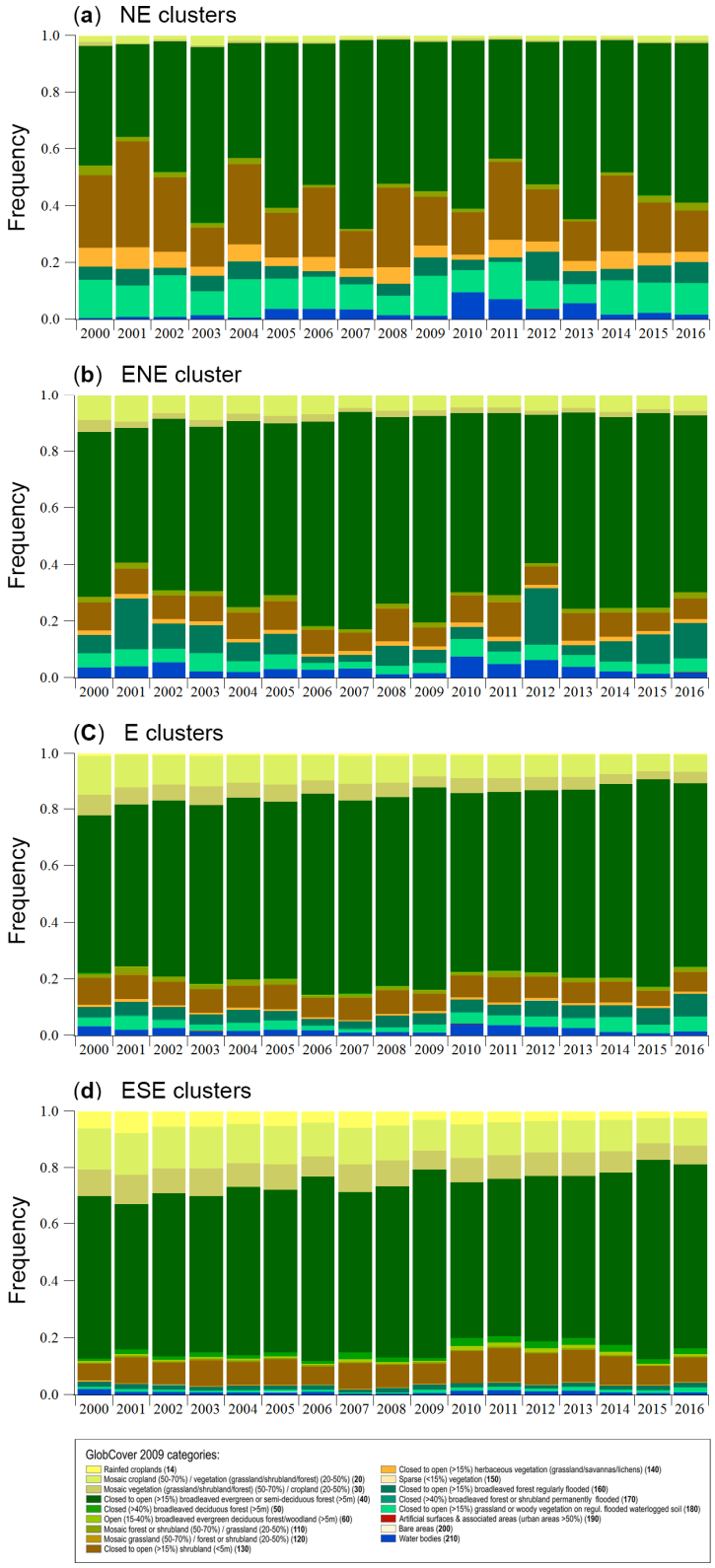

Figure S18. Relative fractions of ATTO-relevant fires (weighted with air mass residence times) within the different land cover categories, discriminated by major BT directions: NE, ENE, E, ESE, and SW. Fire analysis is based on the INPE database (see Sect. S1.1). Results shown here are averages of corresponding year-to-year data (2000-2016) as shown in Fig. S17. Results shown are temporally resolved on yearly basis.

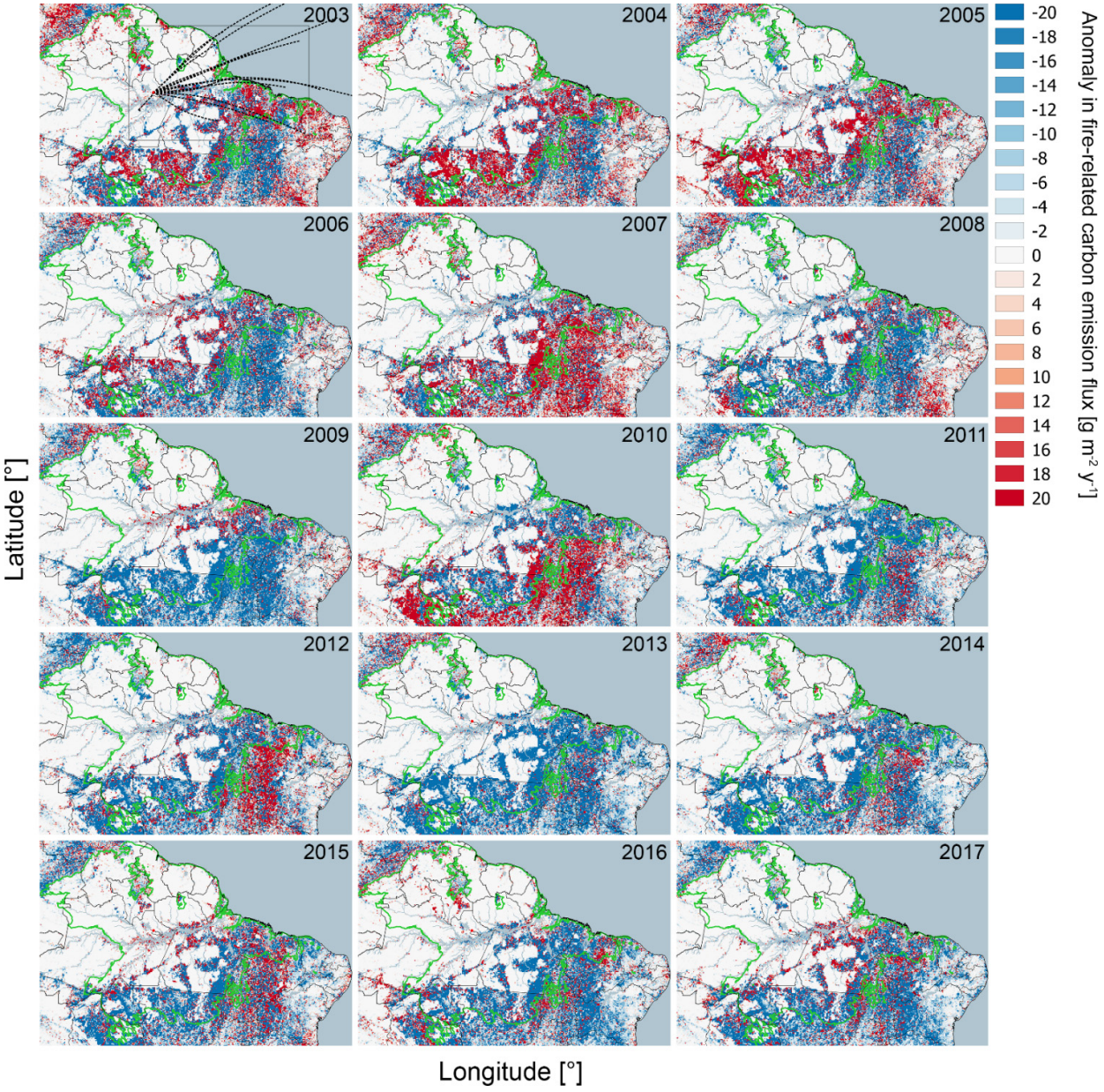

Figure S19. Anomalies in fire-related carbon emission based on GFAS-data for the ATTO-relevant eastern Amazon Basin (ROI_{foot}). Reference time period for anomalies is average from 2003 to 2017. For the year 2003, the BT data is represented as center lines of the 15 BT cluster (black dashed lines, exemplary for year 2003, see Fig. 4). The green line represents the boundaries of the biome of moist broadleaf forests according to Fig. 9.

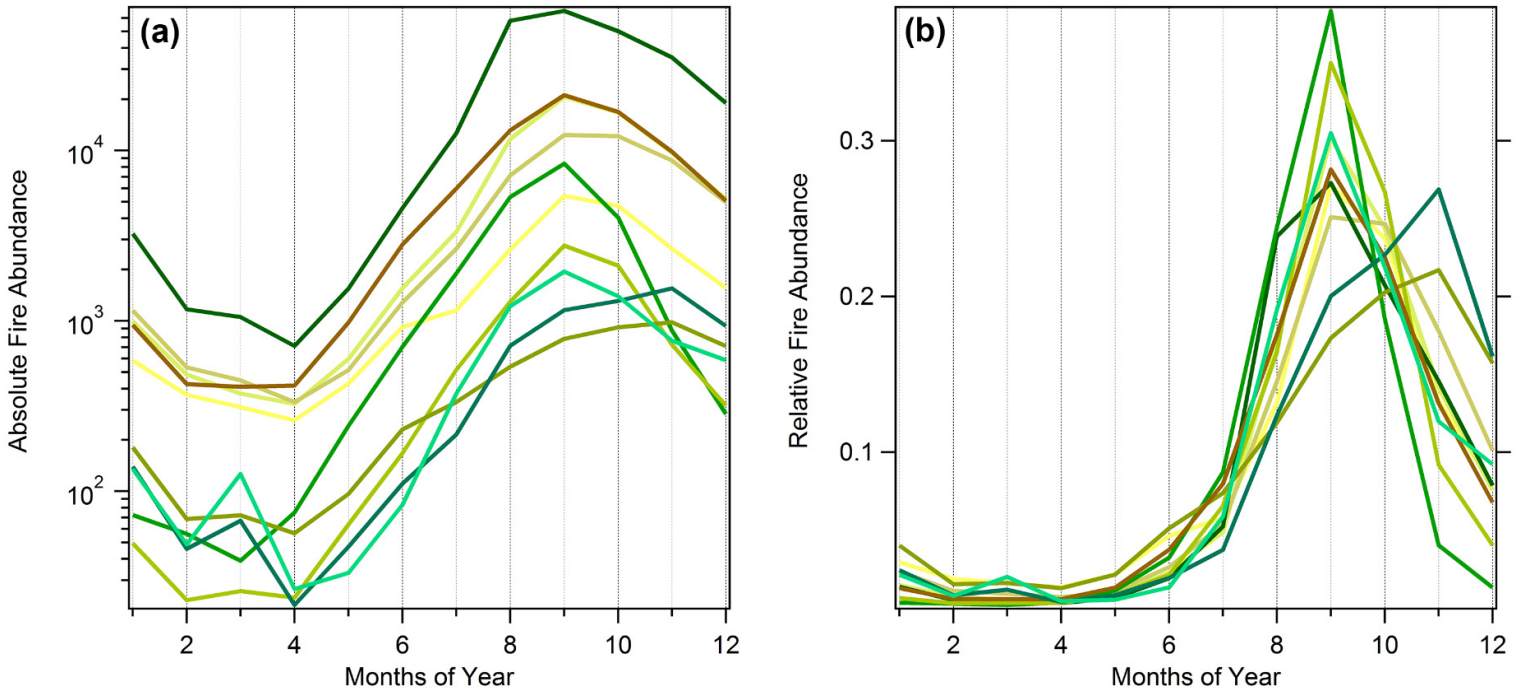

Figure S20. Seasonal cycle of satellite-detected fire activity (INPE data set), categorized by land cover type, in which they are detected. This analysis includes all fires in the ATTO site footprint (represented by the combination of all BT cluster footprints). The fire count was weighted by the BT density and, thus, reflects the distance and relevance of the individual fires for the ATTO site. (**a**) Absolute fire count emphasizes in which land cover category fires are most abundant. (**b**) Normalized seasonal cycles in fire activity, shows a fire maximum in Sep and minimum in Apr. The legend of the GlobCover 2009 color code is shown in Fig. 9.

References

Arino, O., Bicheron, P., Achard, F., Latham, J., Witt, R., and Weber, J.-L.: GLOBCOVER The most detailed portrait of Earth, Esa Bulletin-European Space Agency, 24-31, 2008.

Asefi-Najafabady, S., Rayner, P. J., Gurney, K. R., McRobert, A., Song, Y., Coltin, K., Huang, J., Elvidge, C., and Baugh, K.: A multiyear, global gridded fossil fuel CO2 emission data product: Evaluation and analysis of results, Journal of Geophysical Research-Atmospheres, 119, 10.1002/2013jd021296, 2014.

Congalton, R. G., Gu, J. Y., Yadav, K., Thenkabail, P., and Ozdogan, M.: Global Land Cover Mapping: A Review and Uncertainty Analysis, Remote Sensing, 6, 12070-12093, 10.3390/rs61212070, 2014.

Defourny, P., Schouten, L., Bartalev, S., Bontemps, S., Caccetta, P., De Wit, A. J. W., Di Bella, C. M., Gérard, B., Giri, P., Gond, V., ., and et al.: Accuracy assessment of a 300 m global land cover map : the GlobCover experience, International Symposium on Remote sensing of Environment, Stresa, Italie, 2009-05-04 / 2009-05-08, Agritrop : 552799, 2009.

Farr, T. G., Rosen, P. A., Caro, E., Crippen, R., Duren, R., Hensley, S., Kobrick, M., Paller, M., Rodriguez, E., Roth, L., Seal, D., Shaffer, S., Shimada, J., Umland, J., Werner, M., Oskin, M., Burbank, D., and Alsdorf, D.: The shuttle radar topography mission, Rev. Geophys., 45, 33, 10.1029/2005rg000183, 2007.

Hansen, M. C., Potapov, P. V., Moore, R., Hancher, M., Turubanova, S. A., Tyukavina, A., Thau, D., Stehman, S. V., Goetz, S. J., Loveland, T. R., Kommareddy, A., Egorov, A., Chini, L., Justice, C. O., and Townshend, J. R. G.: High-Resolution Global Maps of 21st-Century Forest Cover Change, Science, 342, 850-853, 10.1126/science.1244693, 2013.

Hijmans, R. J., Cameron, S. E., Parra, J. L., Jones, P. G., and Jarvis, A.: Very high resolution interpolated climate surfaces for global land areas, International Journal of Climatology, 25, 1965-1978, 10.1002/joc.1276, 2005.

Hutchinson, M. F.: Anusplin Version 4.3., in, The Australian National University, Canberra, Australia, Centre for Resource and Environmental Studies, 2004.

Kaiser, J. W., Heil, A., Andreae, M. O., Benedetti, A., Chubarova, N., Jones, L., Morcrette, J. J., Razinger, M., Schultz, M. G., Suttie, M., and van der Werf, G. R.: Biomass burning emissions estimated with a global fire assimilation system based on observed fire radiative power, Biogeosciences, 9, 527-554, 10.5194/bg-9-527-2012, 2012.

Kottek, M., Grieser, J., Beck, C., Rudolf, B., and Rubel, F.: World map of the Koppen-Geiger climate classification updated, Meteorologische Zeitschrift, 15, 259-263, 10.1127/0941-2948/2006/0130, 2006.

Lehner, B., Liermann, C. R., Revenga, C., Vorosmarty, C., Fekete, B., Crouzet, P., Doll, P., Endejan, M., Frenken, K., Magome, J., Nilsson, C., Robertson, J. C., Rodel, R., Sindorf, N., and Wisser, D.: High-resolution mapping of the world's reservoirs and dams for sustainable river-flow management, Frontiers in Ecology and the Environment, 9, 494-502, 10.1890/100125, 2011.

Olson, D. M., Dinerstein, E., Wikramanayake, E. D., Burgess, N. D., Powell, G. V. N., Underwood, E. C., D'amico, J. A., Itoua, I., Strand, H. E., Morrison, J. C., Loucks, C. J., Allnutt, T. F., Ricketts, T. H., Kura, Y., Lamoreux, J. F., Wettengel, W. W., Hedao, P., and Kassem, K. R.: Terrestrial Ecoregions of the World: A New Map of Life on Earth, Bioscience, 51, 933-938, 10.1641/0006-3568(2001)051[0933:teotwa]2.0.co;2, 2001.

Paruelo, J. M., Jobbagy, E. G., and Sala, O. E.: Current distribution of ecosystem functional types in temperate South America, Ecosystems, 4, 683-698, 10.1007/s10021-001-0037-9, 2001.

Quaife, T., and Cripps, E.: Bayesian Analysis of Uncertainty in the GlobCover 2009 Land Cover Product at Climate Model Grid Scale, Remote Sensing, 8, 18, 10.3390/rs8040314, 2016.

Ramankutty, N., and Foley, J. A.: ISLSCP II Potential Natural Vegetation Cover. In Hall, Forest G., G. Collatz, B. Meeson, S. Los, E. Brown de Colstoun, and D. Landis (eds.). ISLSCP Initiative II Collection. Data set. Available on-line [http://daac.ornl.gov/] from Oak Ridge National Laboratory Distributed Active Archive Center, Oak Ridge, Tennessee, U.S.A. doi:10.3334/ORNLDAAC/961, in, 2010.

Rayner, P. J., Raupach, M. R., Paget, M., Peylin, P., and Koffi, E.: A new global gridded data set of CO2 emissions from fossil fuel combustion: Methodology and evaluation, Journal of Geophysical Research-Atmospheres, 115, 10.1029/2009jd013439, 2010.

Rouse, J. W., Haas, R. H., Schell, J. A., and Deering, D. W.: Monitoring vegetation systems in the Great Plains with ERTS. Third ERTS Symposium 1, 309-317, 1973.

Rubel, F., and Kottek, M.: Observed and projected climate shifts 1901-2100 depicted by world maps of the Koppen-Geiger climate classification, Meteorologische Zeitschrift, 19, 135-141, 10.1127/0941-2948/2010/0430, 2010.

Sanderson, E. W., Jaiteh, M., Levy, M. A., Redford, K. H., Wannebo, A. V., and Woolmer, G.: The human footprint and the last of the wild, Bioscience, 52, 891-904, 10.1641/0006-3568(2002)052[0891:thfatl]2.0.co;2, 2002.

Saturno, J., Holanda, B. A., Pöhlker, C., Ditas, F., Wang, Q., Moran-Zuloaga, D., Brito, J., Carbone, S., Cheng, Y., Chi, X., Ditas, J., Hoffmann, T., Hrabe de Angelis, I., Könemann, T., Lavrič, J. V., Ma, N., Ming, J., Paulsen, H., Pöhlker, M. L., Rizzo, L. V., Schlag, P., Su, H., Walter, D., Wolff, S., Zhang, Y., Artaxo, P., Pöschl, U., and Andreae, M. O.: Black and brown carbon over central Amazonia: Long-term aerosol measurements at the ATTO site, Atmos. Chem. Phys. Discuss., 2017, 1-57, 10.5194/acp-2017-1097, 2017.

Soares-Filho, B. S., Nepstad, D. C., Curran, L. M., Cerqueira, G. C., Garcia, R. A., Ramos, C. A., Voll, E., McDonald, A., Lefebvre, P., and Schlesinger, P.: Modelling conservation in the Amazon basin, Nature, 440, 520-523, 10.1038/nature04389, 2006.

Soares-Filho, B. S., Nepstad, D. C., Curran, L. M., Voll, E., Cerqueira, G. C., Garcia, R. A., Ramos, C. A., McDonald, A., Lefebvre, P., and Schlesinger, P.: Modeled Deforestation Scenarios, Amazon Basin: 2002-2050., in, edited by: Oak Ridge National Laboratory Distributed Active Archive Center, O. R., Tennessee, USA, 2013.

Souza, C. M., Siqueira, J. V., Sales, M. H., Fonseca, A. V., Ribeiro, J. G., Numata, I., Cochrane, M. A., Barber, C. P., Roberts, D. A., and Barlow, J.: Ten-Year Landsat Classification of Deforestation and Forest Degradation in the Brazilian Amazon, Remote Sensing, 5, 5493-5513, 10.3390/rs5115493, 2013.

Tyukavina, A., Hansen, M. C., Potapov, P. V., Stehman, S. V., Smith-Rodriguez, K., Okpa, C., and Aguilar, R.: Types and rates of forest disturbance in Brazilian Legal Amazon, 2000-2013, Science Advances, 3, 15, 10.1126/sciadv.1601047, 2017.

Weiss, D. J., Nelson, A., Gibson, H. S., Temperley, W., Peedell, S., Lieber, A., Hancher, M., Poyart, E., Belchior, S., Fullman, N., Mappin, B., Dalrymple, U., Rozier, J., Lucas, T. C. D., Howes, R. E., Tusting, L. S., Kang, S. Y., Cameron, E., Bisanzio, D., Battle, K. E., Bhatt, S., and Gething, P. W.: A global map of travel time to cities to assess inequalities in accessibility in 2015, Nature, 553, 333-+, 10.1038/nature25181, 2018.